Multipixel system for gigahertz frequency-domain optical imaging of finger joints

Uwe J. Netz,[1] Jürgen Beuthan,[1] and Andreas H. Hielscher[2]
[1]*Institut für Medizinische Physik und Lasermedizin, Charité-Universitätsmedizin Berlin, 14195 Berlin, Germany*
[2]*Departments of Biomedical Engineering and Radiology, Columbia University, New York, New York 10027, USA*

(Received 22 August 2007; accepted 15 January 2008; published online 3 March 2008)

Frequency-domain optical imaging systems have shown great promise for characterizing blood oxygenation, hemodynamics, and other physiological parameters in human and animal tissues. However, most of the frequency domain systems presented so far operate with source modulation frequencies below 150 MHz. At these low frequencies, their ability to provide accurate data for small tissue geometries such as encountered in imaging of finger joints or rodents is limited. Here, we present a new system that can provide data up to 1 GHz using an intensity modulated charged coupled device camera. After data processing, the images show the two-dimensional distribution of amplitude and phase of the light modulation on the finger surface. The system performance was investigated and test measurements on optical tissue phantoms were taken to investigate whether higher frequencies yield better signal-to-noise ratios (SNRs). It could be shown that local changes in optical tissue properties, as they appear in the initial stages of rheumatoid arthritis in a finger joint, are detectable by simple image evaluation, with the range of modulation frequency around 500 MHz proving to yield the highest SNR. © *2008 American Institute of Physics.*
[DOI: 10.1063/1.2840344]

I. INTRODUCTION

A. Optical tomography

Considerable progress has been made towards a novel biomedical imaging modality often referred to as diffuse optical tomography (DOT).[1–5] This technology is based on delivering low energy electromagnetic radiation (wavelength $\lambda \sim 650-900$ nm), typically through optical fibers, to one or more location on the surface of a biological tissue under consideration and measuring transmitted and/or back reflected intensities at distances up to ~10 cm at one or more locations. The propagation of light in biomedical tissue is governed by the spatially varying scattering and absorption properties of the medium, which are described in the framework of scattering and absorption coefficients, μ_s and μ_a, given in units of 1/cm. Difference in the refractive index between intracellular and extra cellular fluids, and various subcellular components, such as mitochondria or nuclei, as well as varying tissue densities give rise to differences in μ_s between different tissue.[6–8] Differences in chromophore content and concentration lead to differences in μ_a of different tissue types. Based on measurements of transmitted and reflected light intensities on the surface of the medium, a reconstruction of the spatial distribution of the optical properties inside the medium is performed. From this maps, physiological important parameters such as oxy- and deoxyhemoglobin can be derived. Recently, progress has been made in DOT primarily in the fields of brain imaging,[9–12] breast cancer detection,[13–22] imaging of finger joints,[23–26] and blood oximetry in muscle.[27–29]

B. Imaging modalities

There are several methods in which to perform optical imaging through tissue. Generally, the instrumentation operates in one of three possible modes: steady-state domain [also known as continuous wave (cw) domain], frequency domain, or time domain. In steady-state imaging, the light impinges on the body surface with a constant intensity and the intensity of the light transmitted through different sections of the body is detected. In the frequency domain (FD), the incident light is modulated in the megahertz to gigahertz range, which causes so-called "photon density waves" (PDWs) to travel through the tissue.[30] Detection of amplitude and phase of those PDWs provides information about the damping and the time delay of the wave [Fig. 1(a)]. In the time domain, short light pulses are used to illuminate the body, and the attenuated and broadened pulses, which have traveled through different parts of the tissue, are detected.[31,32] Going from steady-state domain over frequency domain to time domain, the imaging systems become increasingly complex and, hence, the cost for these systems increases. However, with increasing complexity the amount of information available increases too. For example, absorption and scattering properties can be better separated using frequency-domain data when compare to cw data. In general, time-resolved imaging can provide the most accurate images with the highest spatial resolution given the same number of sources and detectors. However, time-resolved imaging usually requires long integration times. Fast changing signals, such as, for example, hemodynamic responses to various stimuli, can be best captured with faster operating steady-

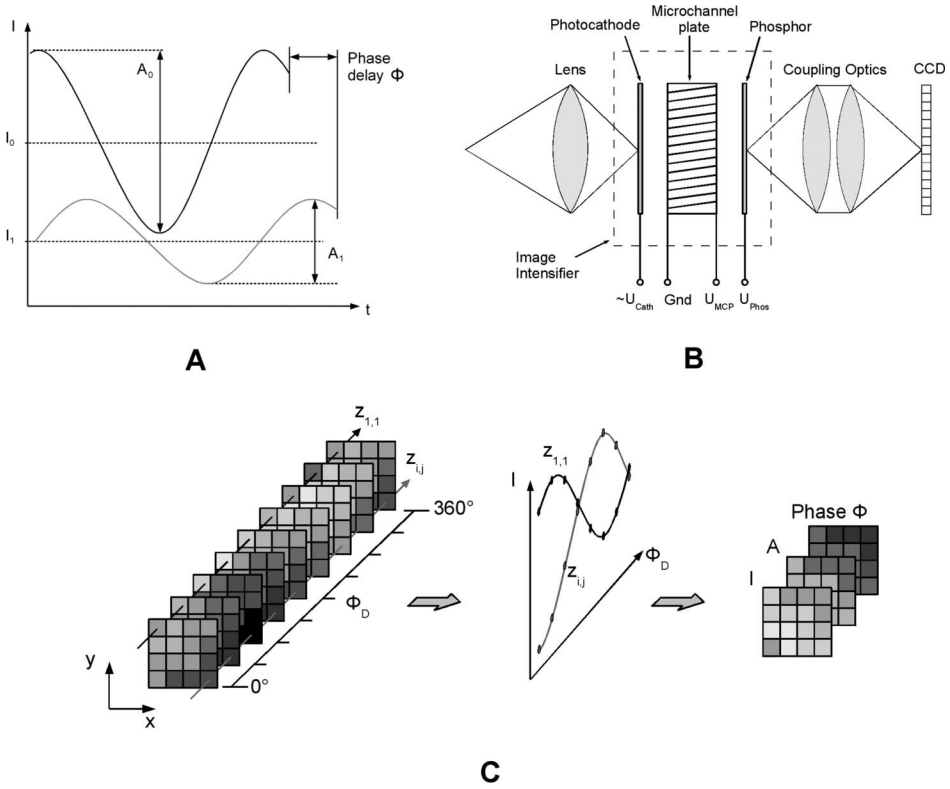

FIG. 1. Scheme for detection of photon density waves (PDW). PDW travelling through tissue (A) undergoes damping in amplitude A and intensity I and some phase delay Φ; an intensified CCD camera (B) is used for two-dimensional detection of PDW. Modulation of the intensifier gain by applying amplitude voltage with PDW frequency to photocathode yields demodulation to a continuous signal on the phosphor screen imaged by a CCD sensor (refer to text). Image acquisition with sequential phase shift by constant phase Φ_D (C) generates stack of images where z profiles are extracted pixelwise for calculation of intensity, amplitude, and phase images.

state systems. For a thorough review of the optical tomographic imaging systems see, for example, references 33–35.

C. Frequency-domain DOT systems

As a compromise between the slow, highly complex, and expensive time-resolved systems, and fast, low cost, limited-resolution steady-state instruments, several groups have developed first clinically useful frequency-domain systems.[17,36–38] In general, one can distinguish two types of approaches: (1) systems that work with multiple single detectors and (2) systems that work with a charged coupled device (CCD) camera and gain modulated intensifiers.

Single detector systems typically use high-gain photomultiplier tubes (PMT) as detectors. Amplitude and phase of the PMT signal are usually derived by heterodyne detection. In this case, the PMT signal is mixed with a reference signal at a frequency $f+\Delta f$ that is slight different from the modulation frequency f of the incident light source. This results in a signal that is modulated at the frequency Δf of typically 1 kHz or more. This signal contains the whole amplitude and phase information of the high-frequency source signal but is much easier to detect and evaluate at the low frequency.[12,17,37–39] Typical measurement errors in phase and amplitude are $\sim 0.5°$ and 1%, respectively. The disadvantage of these systems is that, for tomographic imaging instruments, many of these rather bulky single detectors and their detection electronics need to be assembled, which leads to rather large, complex, expensive instruments. This can be overcome through the use of CCD cameras.

CCD camera systems used for frequency-domain imaging are most often operated in homodyne mode. In this case, a reference frequency is applied to the gain of an image intensifier that is placed in front of the camera. In homodyne mode, the reference frequency is the same as or a harmonic of the source modulation frequency. A steady-state image at the intensifier output is imaged to the CCD. The signal strength in every pixel only depends on the phase difference between the source and detector modulation.[40–42] Sequentially shifting the phase between source and intensifier modulation enables detection of the complete signal oscillation in every pixel and enables reconstruction of amplitude and phase images. The heterodyne mode can also be employed with CCD cameras and works similar as in single detector systems. The frequency $f+\Delta f$ applied to the intensifier has to be a little higher or lower than the modulation frequency f of the light source. This difference frequency Δf has to be chosen well below the maximum frame rate of the CCD so that continuous image acquisition yields image series that contain the complete pixel oscillation from where amplitude and phase can be derived.[43] The first CCD systems, introduced by Berndt and Lakowicz in 1991, used a pulsed laser source at 3.81 MHz and detection of harmonics up to 152.4 MHz.[40,41] Subsequently developed systems used a continuous wave laser diode with sinusoidal modulation of the diode current at 100 MHz.[42,43] Acquisition time for one image series was in the range of several minutes, which was necessary to achieve sufficient signal-to-noise ratio (SNR) by averaging.

D. Current limitations and capabilities

Currently, most imaging systems are limited in their detectable modulation frequency to $f \leqslant 150$ MHz. These systems were designed for imaging of larger media, mostly for breast imaging, where the phase shift, even at low frequencies, is substantial and therefore can be measured with sufficient accuracy. However, there are many applications that

deal with small geometries and small source-detector separation. One example is the fast growing area of small animal imaging and a second example is imaging of finger joints.[24,25] In these cases, large phase shifts that can be measured with sufficient accuracy only emerge at higher frequencies. However, the phase noise is increasing with frequency too.

In previous studies our group[44] and others[45,46] have shown that an optimum modulation frequency exists for which the phase SNR is largest. This optimum frequency may differ depending on the type of tissue and the transillumination geometry. For example, Boas *et al.*[45] performed a theoretical study considering noise in PDW detection. They investigated the effect of the modulation frequency on the detection, localization, and characterization of scattering and absorbing perturbations in a 6 cm thick infinite slab mimicking light propagation in female breast tissue. For characterization of absorbing objects, 0 MHz was found to be the optimal frequency, whereas scattering objects are best characterized at approximately 500 MHz. In another study, involving both theoretical as well as experimental data, Toronov *et al.*[46] analyzed the SNR of changes caused by an absorbing inhomogeneity at different modulation frequencies. Using Monte Carlo simulation of light propagation in the human head and experimental data gained from time domain measurements, they conclude that SNR can be significantly improved by increasing the modulation frequency, with optimal frequencies in the 400–600 MHz range. Finally, a recent theoretical study performed by Gu *et al.*[44] analyzed the SNR of changes caused by optical heterogeneities in a cylindrical volume, which mimics small geometries. Using the frequency-domain equation of radiative transfer, the SNR over a frequency range from 100 to 1000 MHz was analyzed. The authors conclude that, in the cases considered, the best SNR should be achieved with modulation frequencies in the range from 300 to 500 MHz.

Other theoretical and experimental studies concerning frequency-domain imaging performed in the mid-1990s focused on detectability, the achievable contrast, and the resolution of small perturbations in turbid media.[47–49] Patterson *et al.*[47] reported on contrast and resolution derived from line scans over a 5 cm thick slab phantom mimicking female breast containing a 1 cm perturbation with different contrasts in absorption and scattering. From experimental measurements and simulated data at modulation frequencies up to 300 MHz, they conclude that contrast and resolution in amplitude and phase are comparable to dc images, but that amplitude and phase images contain more information about the inhomogeneity and are very sensitive to its position. Using experimental and theoretical data, Krämmer *et al.*[48] analyzed the normalized amplitude and phase shift of transmission line scans across a 0.4 cm absorber in a 4 cm thick fluid phantom with different optical properties looking at modulation frequencies ranging from 60 to 500 MHz. In the case of weak background absorption, resolution and contrast in amplitude and phase images show clear frequency dependence whereas at strong background absorption frequency dependence was negligible. They conclude that, for selecting an optimized modulation frequency, a compromise has to be found between phase shift contrast and detected amplitude, because of nearly linear increase of phase and decrease of amplitude. Further investigations at a 5.5 cm breast mimicking slab phantom were performed by Montandon *et al.*[49] They were able to detect 0.5 cm perturbations in amplitude and phase images at 100 MHz with contrast from 2.0 in both absorption and scattering.

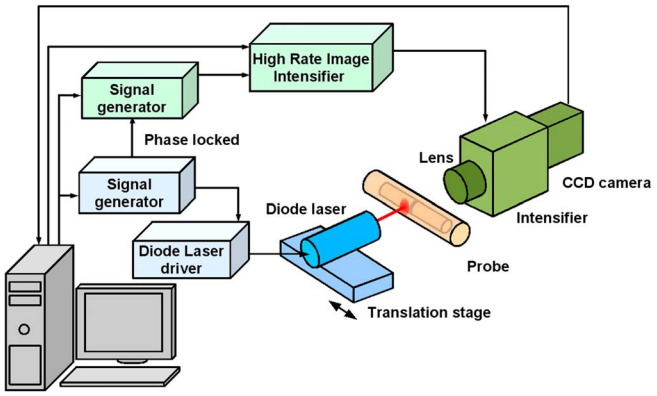

FIG. 2. (Color online) System layout for two-dimensional imaging in the frequency domain.

Overall, these studies suggest that in the case of small geometries source modulation frequencies well beyond 150 MHz can provide much better SNR in the data and, hence, image reconstruction results will be improved. Frequency-domain systems that operate well beyond 150 MHz are therefore highly desirable.

E. Outline of this paper

In this work we present a CCD camera based system that allows for fast acquisition of frequency-domain data up to 1 GHz. The system was designed with application to joint imaging in mind. In the following we will first provide a detailed description of the system's design. This is followed by a thorough characterization of various system parameters, such as frequency-dependent signal-to-noise figures and measurement precision. To test the system for application in joint imaging, we have developed a finger phantom. A discussion concludes the paper.

II. INSTRUMENT DESIGN

A. Overall system layout

The instrument is designed for fast two-dimensional imaging of modulated light transmitted diffusely through a finger joint. The main components of the system are the illumination part, the detection system, and the modulation sources for the light source and detector (Fig. 2). The master signal generator gives ac input to the laser diode driver that supplies the laser diode in the near-infrared range with bias and ac current. The laser illuminates the surface of the object to investigate and the horizontal position is adjusted by moving the laser with a translation stage. The modulated light transmitted through the object is imaged by a lens to an intensified CCD (ICCD) camera. The gain of the ICCD is modulated by the slave signal generator at the same frequency as

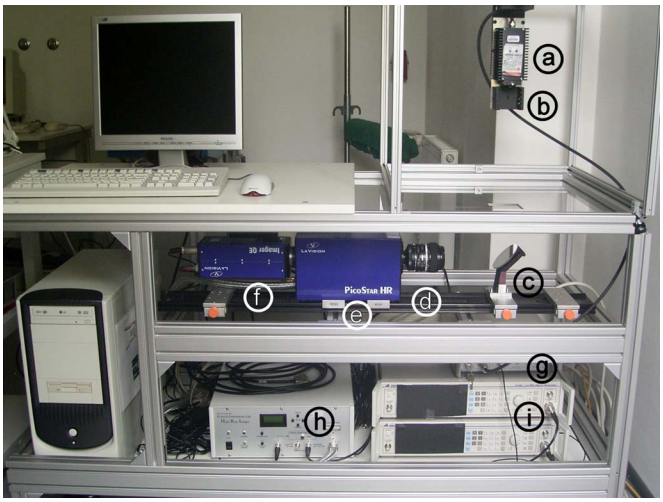

FIG. 3. (Color online) Frequency-domain system composed of (a) diode laser, (b) neutral density filter holder, (c) 45° turning mirror, (d) lens, (e) image intensifier, (f) CCD camera, (g) diode laser driver, (h) high rate image intensifier controller, and (i) signal generators for modulation of laser and intensifier.

the laser. Master and slave signal generators are linked together and phase delay is adjustable. For different phase delays, multiple images are taken and are transferred to a computer. The system is controlled via a graphical user interface. From the stack of images, two-dimensional amplitude and phase images are calculated. All components are described in detail in the following sections.

The system is intended for tomographic imaging of finger joints in a clinical environment later. Therefore, beside high resolution and signal-to-noise ratio, important requirements to meet are an ergonomic and patient friendly hand rest and short data acquisition time. The hand should rest relaxed horizontal on a table top. Thus, the source and detector were arranged in such a way that the laser illuminates and scans the finger from above and the detector is placed underneath the hand to image the transmitted light (Fig. 3).

B. Light source

The light source is a thermoelectric controlled laser diode (LDH-M-C-670, PicoQuant GmbH, Germany) with average optical power of 8 mW at the wavelength $\lambda = 670$ nm (Fig. 3). The output power of the laser diode is stabilized by a feedback loop working on the difference between the laser power setting and the monitor diode current. At the laser diode driver (MDL 300, PicoQuant GmbH, Germany), the average optical power can be adjusted and is displayed as a percentage of the maximum power level. The driver provides the dc bias current and external modulation of optical power with frequencies in the range from 100 kHz to 2 GHz. The cutoff frequency (−3 dB) for optical power is at 875 MHz; at 1 GHz the power is attenuated by nearly 5 dB. The external source of modulation is provided by a signal generator (2023A, Aeroflex Incorporated, Plainview, New York, USA) covering a frequency range from 9 kHz to 1.2 GHz. The modulation depth can be linearly adjusted to 100% of the cw-laser power by adjusting the voltage of the external modulation signal and by the modulation depth control at the driver.

The laser driver flashes a light emitting diode (LED) when modulation depth reaches more than 80% of the cw power to avoid clipping of the modulation amplitude. The laser beam is internally collimated and shows an elliptical beam shape as it is typically for laser diodes. The beam diameter is narrowed by a 1 mm pinhole aperture. The diode laser is vertically mounted on a linear translation stage providing a manual scanning over 4.5 cm.

C. Detection unit

The detector system is an ultrafast gateable ICCD camera that provides rf modulated light amplification up to 1 GHz (PicoStar HR12, LaVision GmbH, Germany). The ICCD system is composed of an optical lens and an intensifier whose output is imaged to a CCD camera. Because of the long construction form of the ICCD system, it is arranged on a horizontal optical bank under the table top and a 45° turning mirror is used. The light from the bottom of the object is imaged to the intensifier with an optical zoom lens adjusted to a focal length of $f = 75$ mm with f stop of 4.8.

The photocathode (S25) at the entrance window of the intensifier converts light into electrons [Fig. 1(b)]. Between the photocathode and a single stage microchannel plate (MCP), a negative voltage U_{cath} accelerates electrons to the front surface of the MCP. The illuminance of the photocathode must not exceed a certain light level because the photocathode could be damaged by inner ion bombardment. In the microchannels electrons are amplified by electron multiplication depending on the high voltage U_{MCP} in the range from 260 to 850 V, where gain varies from 0.01 to 500 and a gain of 1 is reached at 450 V. All electrons leaving the MCP are accelerated towards a phosphor screen (P43) by voltage U_{Phos}, where they are converted into light again. The light emitted from the phosphor is finally imaged by a lens system to the CCD camera. The parameters of the intensifier are controlled by the high rate image intensifier controller (HRI, Kentech Instruments Ltd., England). The electrical field between photocathode and MCP is the object of sinusoidal rf modulation by a second signal generator (2023A, Aeroflex Incorporated, Plainview, New York, USA) for demodulation of light oscillation. The modulation depth can be adjusted by the voltage of external modulation signal and by an additional rf gain at the HRI set as a percentage. The signal generator for signal demodulation (slave) is linked by a 10 MHz signal to the signal generator for light modulation (master). The phase delay between master and slave signal generator is adjustable.

The CCD camera is based on a 1376(h) $\times$ 1040(v) pixel chip with a Peltier cooler and a 12 bit at 16 MHz analog to digital (A/D) converter. A pixel binning on the chip is enabled up to 8(h) $\times$ 128(v). The readout is 10 frames per second for full frame (20 frames at 2×2 binning).

The technical specifications that mainly determine system performance are summarized in Table I.

TABLE I. Technical specifications of system components.

Parameter	Value
System sensitivity (max.)	40 counts/photon at 675 nm
Quantum efficacy intensifier	9.6% at 675 nm
Max. illuminance	10 mlux
System dynamic	2.4×10^5 (108 dB)
CCD A/D converter	12 bit at 16 MHz

D. System control

The ICCD camera, the HRI, and the signal generators are controlled by a computer (CPU Intel Pentium 4, 3.2 GHz). The CCD camera is triggered and read out by an expansion board. HRI and signal generators are controlled via RS232 interface. The measurement and data processing is mainly automated using customized imaging software (DAVIS 7, LaVision GmbH, Germany). The software provides a graphical user interface and enables control of all important parameters of signal generators, HRI, intensifier, and CCD camera, triggers image acquisition, and provides data processing for generation of amplitude and phase images. For safety reasons, the software does not allow exposure times of the CCD camera below 20 ms. This is because the camera image should enable visual control of the actual illuminance to avoid damage of the photocathode. That means that, at normal intensifier gain, the camera image should reach saturation before the illuminance reaches the specified maximum. Normal intensifier gain means MCP voltage not below 670 V at 20 ms.

E. System operation

The PDW reaching the ICCD after traveling through the illuminated object is damped and delayed in phase. Demodulation of the PDW is accomplished in homodyne mode. Amplitude and phase images thus obtained need to be calibrated with respect to two-dimensional inhomogeneities of the two-dimensional detection system. To derive amplitude damping and phase delay caused only by the illuminated object, amplitude and phase are referenced to the source modulation.

1. Demodulation technique

The demodulation of the signal works in a way similar to stepwise scanning of the signal with a periodical gate. By modulation of the photocathode voltage with the same frequency as the laser modulation, only such areas in the image are periodically amplified where light modulation is in phase with photocathode modulation. Therefore, the number of electrons amplified by the MCP oscillates with the modulation frequency and with the amplitude, which depends on the phase. Because the decay time of the phosphor screen is much too long to follow the megahertz oscillation, the light that reaches the CCD camera is constant in time. Thus, the CCD camera generates an image where only areas are bright where the light modulation is in phase with the photocathode modulation. Shifting the phase between the two modulation sources consecutively leads to scanning of the oscillation at every pixel. By sequential phase adjustment over the range of 2π in N steps and repeated image acquisition, the whole period of oscillation is scanned for every pixel of the CCD [Fig. 1(c)]. This stack of images generated in the acquisition cycle is analyzed in the frequency domain. A one-dimensional, fast Fourier transformation (FFT) is performed for every CCD pixel vertically through the stack of images. Subsequently, images are calculated of average intensity I, amplitude A, and phase Φ in the range from $-\pi$ to π, from the complex FFT components.

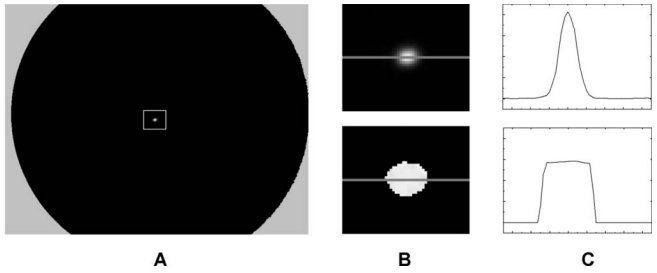

FIG. 4. Image of the laserspot (A), image parts (B) from the marked rectangle for amplitude (top) and phase (bottom), profiles (C) at the marked line of amplitude (top) and phase (bottom).

2. Calibration procedure

The measured intensity, amplitude, and phase values of the PDW contain the response of the source and detector system,

$$I_{\text{measured}} = I_{\text{object}} \cdot I_{\text{system}},$$

$$A_{\text{measured}} = A_{\text{object}} \cdot A_{\text{system}},$$

$$\phi_{\text{measured}} = \phi_{\text{object}} + \phi_{\text{system}}. \quad (1)$$

Here, "object" means the signal generated by the object and "system" refers to the signal generated as it would be without any object. Furthermore, the response of the photocathode and the light transmittance of the lens are not uniform over the whole area but show some kind of vignetting depending on the frequency. Thus amplitude, intensity, and phase images need to be calibrated in respect to nonuniformity and referenced to the laser source to obtain the amplitude damping and phase shift for the measured object only.

At first, the amplitude and phase of the source have to be determined by directly imaging the laser spot on the CCD (Fig. 4). Because the unattenuated laser intensity is much too high and would cause damage of the intensifier, appropriate neutral density filters are used to diminish laser power. To image the laser spot, a sheet of white paper was inserted as a diffusing screen in the object plane. After performing the FFT to analyze the laser spot, the amplitude image shows a typical Gaussian-shaped profile over the laser spot whilst the phase is nearly constant over the spot area [Fig. 4(b) and 4(c)]. From the images, the coordinates (x_S, y_S) at maximum of A and values A_S and I_S at these coordinates are determined first. The phase Φ_S of the laser spot is determined by averaging the phase in a region of interest (ROI) of $11\times11 = 121$ pixels around (x_S, y_S). Because of the filter and the diffusing screen, A and I are damped by a constant factor F,

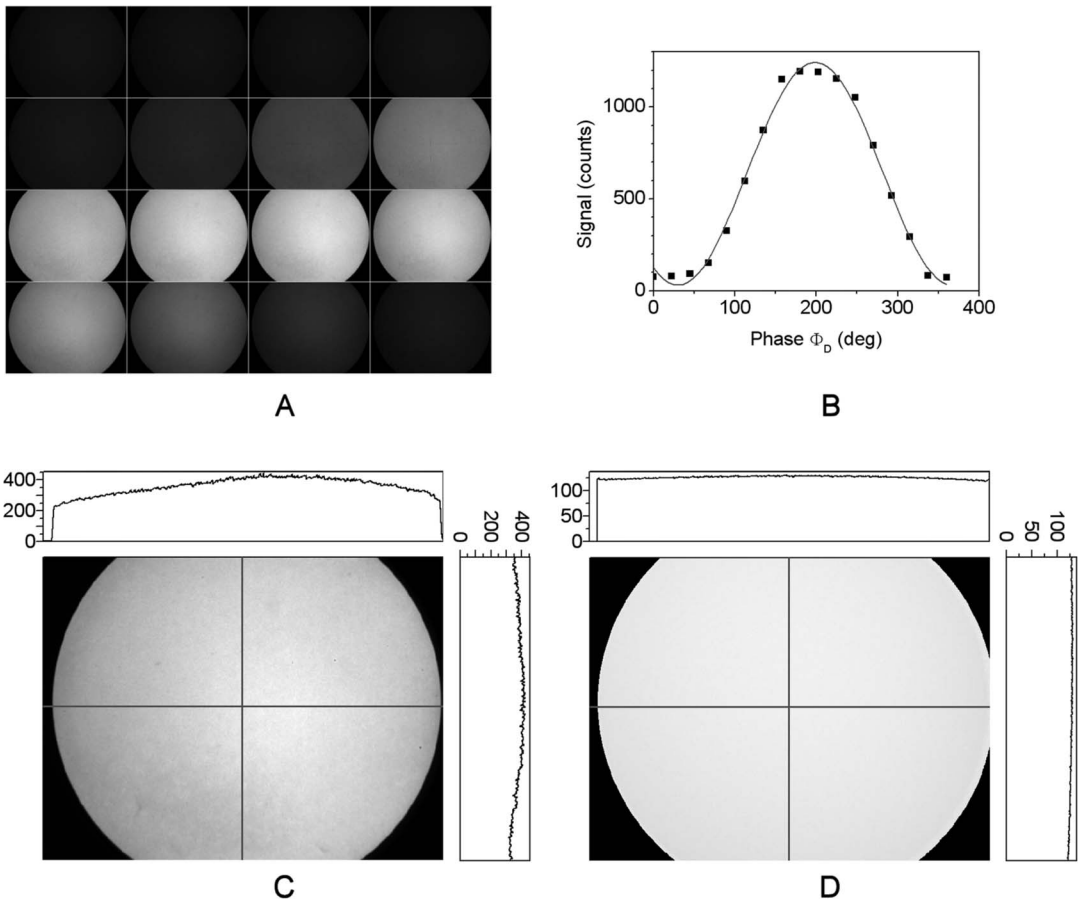

FIG. 5. Homogeneous illumination for calibration purpose at 500 MHz, stack of 16 images with different phases Φ_D (A), z profile of intensity oscillation fitted by sine function (B), amplitude (C), and phase image (D) with x and y profiles.

$$A_S = \max[A_S(x,y)] = F \cdot A_{\text{system}},$$

$$\Phi_S = \langle \Phi_S(x,y) \rangle = \Phi_{\text{system}}. \tag{2}$$

The impact on the phase of the filter and the thin diffusing screen could not be detected and is negligible here.

For calibration with respect to nonuniformity, the lens is illuminated nearly homogeneously by inserting two sheets of white paper as diffusing screens between laser and intensifier. The first diffusing screen is placed in the object plane that causes diffuse broadening of the laser beam. The second screen is placed near to the lens. This leads to very unsharp imaging of the second diffusing screen onto the photocathode and homogeneous illumination. To verify the homogeneity of illumination, the laser diode was moved laterally. If the illumination is not homogeneous, the shape of the amplitude and phase distribution in the images is caused by the laser spot profile and the distribution should change with laser position. After normalization of the images for different laser positions, no substantial changes of the shape of signal distribution in the images could be found. The resulting calibration images A_{cal}, I_{cal}, and Φ_{cal} (Fig. 5) are referenced to the source, so that at the spot position, calibration images have amplitude and phase values of the laser spot,

$$A_{\text{calL}}(x,y) = \frac{A_{\text{cal}}}{A_{\text{cal}}(x_S,y_S)} A_S,$$

$$\Phi_{\text{calL}}(x,y) = \Phi_{\text{cal}} - \Phi_{\text{cal}}(x,y) + \Phi_S. \tag{3}$$

Subsequently, every amplitude and phase image of the measured object is calibrated to this photocathode response by division of A and subtraction of phase,

$$A(x,y) = \frac{A_{\text{measured}}(x,y)}{A_{\text{calL}}(x,y)} = F \cdot A_{\text{object}}(x,y),$$

$$\Phi(x,y) = \Phi_{\text{measured}}(x,y) - \Phi_{\text{calL}}(x,y) = \Phi_{\text{object}}(x,y). \tag{4}$$

Correction of intensity is carried out in the same way as for amplitude.

III. SYSTEM CHARACTERIZATION

For characterization of the system performance, we applied homogeneous illumination to the lens. That enables statistical evaluation of signal and noise over a certain number of pixels in a ROI in the images. First, we investigated the dependence of signal and noise in the images on the different adjustable system parameters to find out which are the parameters that affect the signal quality. Subsequently, the system performance was investigated with respect to the frequency behavior and precision. Finally, the system was tested with measurements at different phantoms to determine

the sensitivity for representation of inhomogeneities or changes in the tissue with regard to imaging of finger joints.

A. System performance

1. Signal and noise

Only a few photons on the intensifier are necessary to generate a signal on the CCD. However, the signal strength in the images depends not only on the optical intensity focused to the intensifier entry but on the gain of the different amplification stages of the ICCD, too. Therefore, several parameters influence the signal level. The average light intensity is adjusted by the optical power of the laser. The amplification is adjusted by the voltage settings at the intensifier, mainly by U_{cath} and U_{MCP}, and by exposition time and factor of pixel binning on the CCD. The quality of detecting phase-resolved modulation depends on the depth of the laser modulation, the modulation of intensifier amplification, and the number of phase steps in a demodulation cycle.

The main source of noise is shot noise (quantum noise) and readout noise of the CCD. For short exposure times (in the millisecond range), the thermal noise caused by the photocathode and the cooled CCD is very low and, therefore, is negligible and can be disregarded. Shot noise here is generated mainly in multiple conversions between light and electrons in the intensifier and on the CCD chip. It increases with the square root of the number of particles generated. Therefore, increasing laser optical power, amplification, exposure time, and binning yield improved SNR. To minimize the contribution of readout noise, the whole dynamic range of the CCD should always be used. This is achieved too by increasing laser optical power, intensifier amplification, exposition time, and pixel binning.

Considering the SNR in the detection of PDWs, the modulation of laser and intensifier should be as high as possible. The number of phase steps determines accuracy of amplitude and phase calculation by the Fourier transform. Thus, with an increasing number of steps, noise is reduced in amplitude and phase images. Binning reduces resolution but decreases noise and image acquisition time because several pixels are read out together in one step.

Laser modulation and intensifier demodulation are both limited in performance for frequencies approaching 1 GHz, and the signal deteriorates with increasing frequency. Therefore, the optimal parameter set for modulation and demodulation varies over the frequency range.

2. System specification

We investigated the dependence of the SNR for amplitude and phase on all system parameters. To enable measurement of system signal and noise, the lens was illuminated homogeneously by inserting diffusing screens in the optical path. The laser optical power was attenuated by neutral density filters to a level compatible to the sensitivity of the intensifier. At first, a dark image was taken and subtracted from all further images to correct for CCD offset. The SNR was determined by calculating signal and noise from mean and standard deviation σ for amplitude and phase in a ROI of $11\times11=121$ pixels at the center of the image.

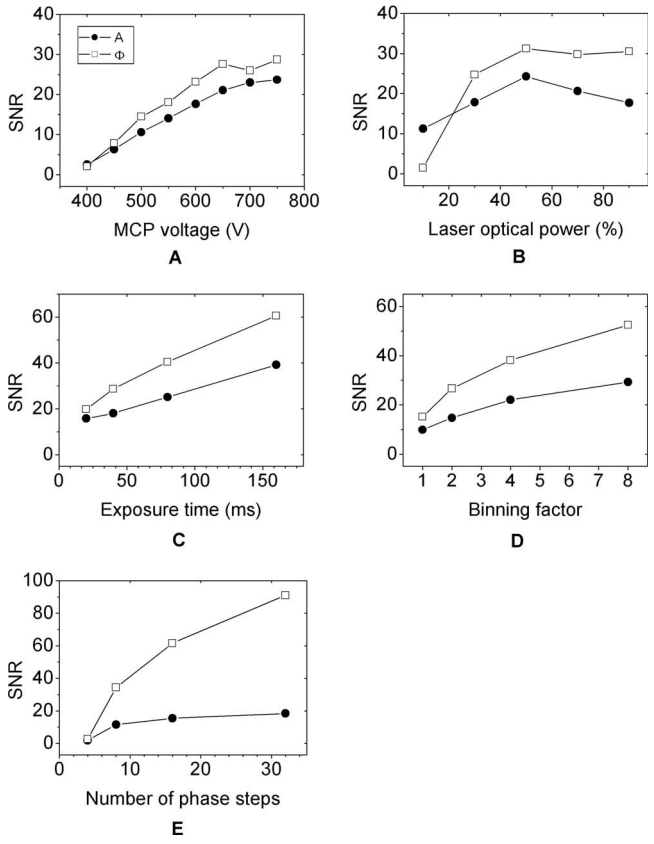

FIG. 6. Signal-to-noise ratio of amplitude and phase for homogeneous illumination of ICCD at 500 MHz, evaluated from mean and standard deviation in ROI over 11×11 pixels in center of images, for alteration of various parameters: MCP voltage (A), laser optical power (B), CCD exposure time (C), pixel binning (D), and number of phase steps (E).

To determine how the SNR is influenced by the different system parameters, first the SNR is measured for a fixed standard parameter set. Then for every single parameter, the change of SNR was determined when changing only this single parameter. Hence, the dominant parameters to influence SNR were found to be the MCP voltage, laser optical power, exposure time, binning, and number of phase steps. In Fig. 6 the SNR dependence on variation of these parameters over a wide range is shown. As expected the SNR increases with increasing MCP voltage, laser optical power, exposure time, binning, and number of phase steps. Only the dependence on laser optical power shows some saturation and a maximum at 50% power. The optical power at 50% behind the 1 mm pinhole aperture was measured to be 2 mW, which equals ~3 mW/mm^2. However, having future clinical trials in mind, for patient security, the maximum permissible exposure for skin at the finger surface must not exceed 2 mW/mm^2 at $\lambda=670$ nm (ANSI Z136.1-2000).

To find an optimal set of parameters, it is not possible to set all parameters to their value with maximum SNR because signal amplification would be much too strong. Because improvement of SNR by means of exposure time and number of phase steps involves raising the acquisition time, these parameters should be set to relatively low values to achieve minimum time required for an acquisition cycle. The pixel binning should be advanced as long as the spatial resolution stays sufficient. The CCD full capacity can always be used by increasing the MCP voltage.

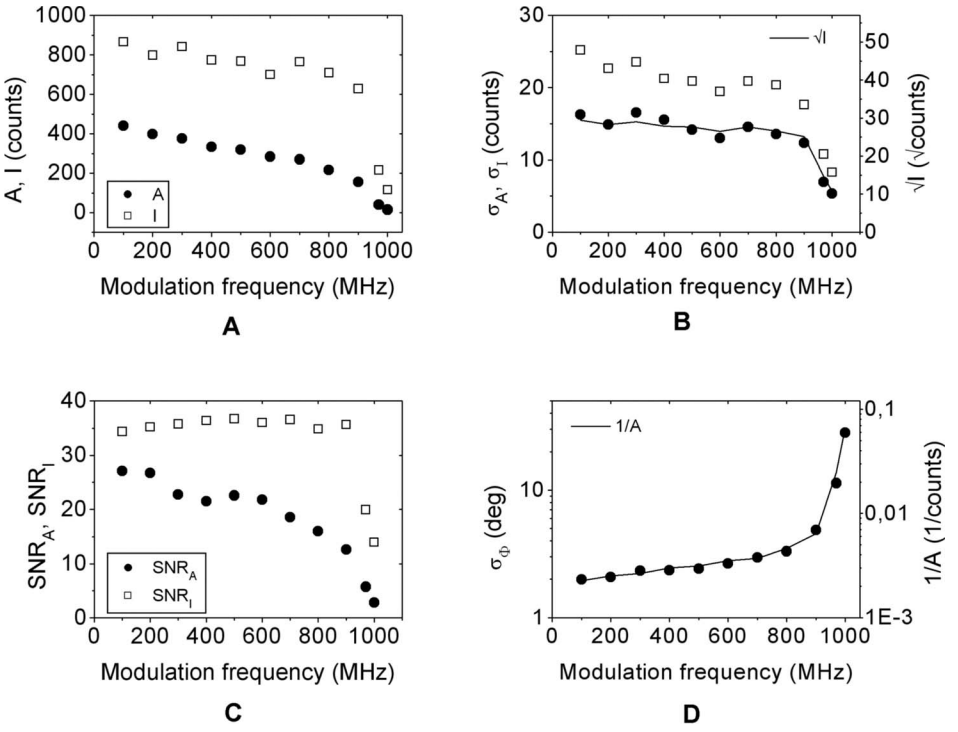

FIG. 7. Signal response over the whole frequency range for homogeneous illumination, evaluated in ROI of 11×11 pixels in center of images: Amplitude and intensity signal from mean value (A), noise of A and I from standard deviation σ with root of intensity signal (line) fitted to amplitude noise (B), amplitude and intensity signal-to-noise ratio (SNR) (C), and phase noise from standard deviation σ with reciprocal of A fitted in (D).

3. System frequency response

First, for investigation of the system frequency response, only neutral density filters and diffusing screens for homogeneous illumination were inserted into the optical path. The system parameters were adjusted for enabling measurements over the whole frequency range with sufficient signal strength and kept constant for all frequencies. The exposure time was set to 80 ms, an acquisition cycle was divided into 16 phase steps, and the MCP voltage was set to 680 V. A pixel binning of 2×2 and field of view of 85 mm in the object plane yield a resolution of 7.85 pixel/mm. The average optical power of the laser was set to 10% at 100 MHz. The frequency range was 100–1000 MHz with steps of 100 MHz. To evaluate signal and noise at the center of the image, mean and standard deviations σ for A, I, and Φ were calculated in a certain ROI of $11\times11=121$ pixels.

The frequency response can only be determined with respect to phase noise and stability but not with respect to the absolute system phase, because the phase between signal generators changes every time that a new frequency is adjusted and is therefore more random. The software only controls the phase shift between the two signal generators. Thus, only relative phase changes can be measured.

Amplitude and intensity signals show a moderate decrease from 100 to 900 MHz and a sharp decline above [Fig. 7(a)]. The noise σ_A and σ_I also decreases with increasing frequency [Fig. 7(b)]. Here, σ_A is proportional to square root of I as predicted in the work of Toronov *et al.*[46] The SNR_I remains constant around 36 until 900 MHz and declines at 1000 MHz, whereas SNR_A decreases with increasing frequency from 27 to 3. Phase noise σ_Φ increases slightly until 800 MHz and steeply above from 2° to 28°. The course of σ_Φ is nearly proportional to the reciprocal of A as predicted by Toronov *et al.*

4. Precision

The precision of a system depends on the stability of the signal. The precision was determined by repeated measurement throughout a period of 30 min. The measurement was repeated 11 times every 3 min under the same conditions as before. For every measurement, the mean in the ROI was determined and the standard deviation of this mean over all measurements was calculated. Precision δ was defined to this standard deviation.

Precision δ_A and δ_I decreases with increasing frequency [Fig. 8(a)]. The coefficient of variation (CV), i.e., precision divided by signal, in amplitude is about 2%–5% with a steep increase to over 10% at 1000 MHz. Precision δ_Φ of the phase is around 1° and increases above 800 MHz [Fig. 8(b)]. To show the uniformity of precision over the whole area of the intensifier, precision images of amplitude and phase at 500 MHz were calculated. For this purpose, the original amplitude and phase images from repeated measurements were completely divided into regions of 11×11 pixels. The mean

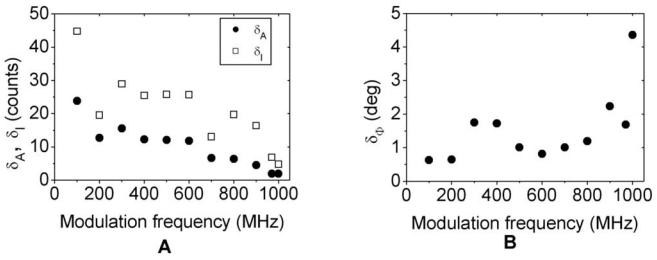

FIG. 8. Precision of amplitude (A) and phase (B) evaluated with homogeneous illumination from repeated measurement every 3 min (11 times) for a total of 30 min, evaluated by calculating the mean in an ROI of 11×11 pixels in center of every image and standard deviation of mean values over the stack of images.

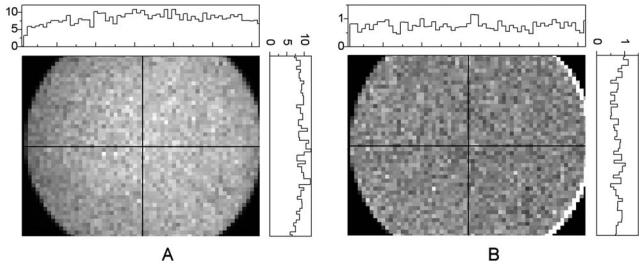

FIG. 9. Precision images of amplitude (A) and phase (B) at 500 MHz. The original amplitude and phase images from 11 times repeated measurement in 30 min were completely divided into regions of 11×11 pixels. Mean was calculated in every region and precision was determined from standard deviation of mean over the stack of 11 images. Finally, new images were built from precision values, profiles were extracted at marked lines.

was calculated in every region and the precision was determined from the standard deviation of the mean over the stack of 11 images. Finally, new images were calculated from precision values (Fig. 9). The profiles extracted on horizontal and vertical center lines show some variance but no major deviation over the whole intensifier area.

5. Data acquisition time

The time required to complete a whole scan of the light source for tomographic data generation consists of the image acquisition time, phase adjustment, translation of the light source, and data storage. With regard to use in a clinical environment, the time for complete data acquisition should be kept below 1 min. With eight phase steps, 2×2 binning, and 40 ms exposure time, an image acquisition cycle can be completed in about 1.6 s. Assuming motorized scanning of the light source of over 20 mm with mean translation speed of 1 mm/s and 11 source positions leads to a total acquisition time of less than 40 s.

B. Phantom test

For characterization of the system sensitivity to local variations of optical properties inside a medium, we developed two kinds of phantoms: a homogeneous slab phantom with a small inserted layer and a detailed finger joint phantom.

1. Homogeneous slab phantom

Phantom design. The slab phantom serves as a highly abstracted finger joint phantom with the layer representing a perturbation to be detected. It was built with a thickness of 20 mm, which relates to typical finger thickness, and with lateral dimensions high enough to avoid boundary problems in transillumination (x, y, $z=80\times70\times20$ mm^3, see Fig. 10). The material used was silicone (Elastosil® RT 601, Wacker Chemie AG, Germany). This is a two component material that is processed in the liquid phase before it hardens after some hours. It is clear without significant absorption or scattering in the visible and near-infrared spectra and has a refractive index of $n=1.41$. We added homogeneously distributed TiO_2 (titanium dioxide) powder as scattering particles and a special silicone dye (Silopren LSR, GE Bayer Silicones, Germany). To investigate the system sensitivity to

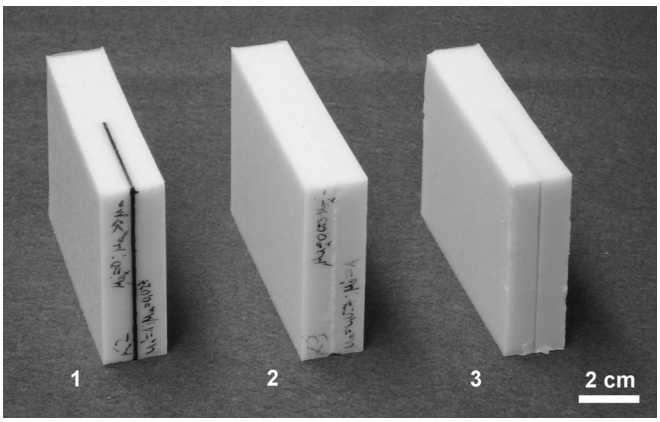

FIG. 10. Solid phantoms in slab geometry made of silicone. All phantoms have the same background optical properties but an inserted layer with optical properties differing from background: totally absorbing (1), background properties but doubled scattering (2), and background properties but doubled absorption (3).

perturbations, we inserted a 1 mm thin layer of the same material into three phantoms in the xy plane. This was done in a two-step pouring process. Each layer was bounded by an edge in the middle of each phantom in the x direction. The optical properties of the layers were adjusted so that one layer was nearly totally absorbing and two layers had the background optical properties but doubled absorption or scattering (Table II).

Frequency response. To test the performance during measurements on tissuelike media, the frequency response was evaluated at the homogeneous part of the slab phantom. The source was placed 20 mm away from the edge of the inserted layer to avoid its influence on radiation transport. Image analysis was carried out opposite the laser source position over an ROI of $11\times11=121$ pixels which is equivalent to approximately 2 mm^2 on the phantom surface. Parameters were set to 80 ms exposure time, 2×2 binning, 16 phase steps, 670 V in MCP voltage, and 10% laser power at 100 MHz.

Figure 11 shows the signal, noise σ, and SNR of amplitude, intensity, and phase. To show the performance of the

TABLE II. Optical properties of phantom components.

	Scattering μ_s' (cm^{-1})	Absorption μ_a (cm^{-1})
Slab phantom:		
Background	10.0	0.27
Layer 1	10.0	120.0
Layer 2	20.0	0.27
Layer 3	10.0	0.54
Finger phantom:		
skin complex	10.0	0.15
bone	10.0	0.4
capsule:		
healthy	3.0	0.8
inflamed	6.0	1.2
joint fluid:		
healthy	0.04	0.05
inflamed	0.16	0.13

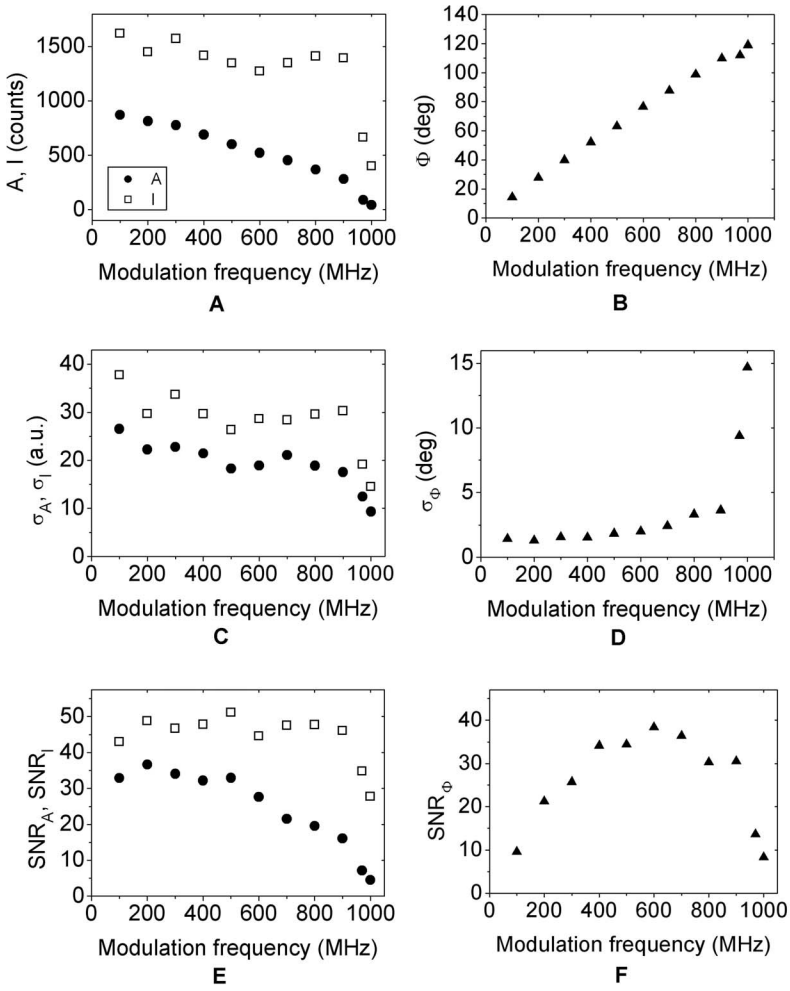

FIG. 11. Transmission at homogeneous part of slab phantom with layer 2, far from boundaries and edge of the layer, evaluated in ROI of 11×11 pixels in the images opposite the laser source: signal [(A) and (B)], noise [(C) and (D)], and SNR [(E) and (F)] for amplitude, intensity, and phase with phase relative to system phase.

system, amplitude and intensity are displayed as raw data without calibration. The phase was referenced to the laser spot (system phase), which was measured ten times and averaged. The intensity I shows a moderate decrease till 900 MHz and then a sudden drop [Fig. 11(a)]. As σ_I behaves in nearly the same way [Fig. 11(c)], the SNR_I is nearly constant, slightly below a value of 50, but decreases rapidly above 900 MHz [Fig. 11(e)]. The amplitude A decreases over the frequency range [Fig. 11(a)] and σ_A decreases slightly too [Fig. 11(c)]. Therefore, the SNR_A decreases over the whole frequency range from around 35 to 5 [Fig. 11(e)]. The phase delay Φ caused by the phantom shows an expected increase with increasing frequency [Fig. 11(b)] from 14° to 119°. Noise σ_Φ behaves very similar to measurements with homogeneous illumination [Fig. 11(d)]. In Fig. 11(f) one can see that the SNR_Φ shows first an increase and at higher frequencies a decrease, which results in a maximum of $\mathrm{SNR}_\Phi=38$ around $f=500-600$ MHz. This is in good agreement with theoretical and experimental investigations.[44,50]

Edge response. The slab phantom with a totally absorbing layer was manually scanned using the source along a line over a range from −20 to +20 mm, with step width of 2 mm (Fig. 12). The edge of the layer is located at position of 0 mm. Measurements were performed for 100, 500, and 1000 MHz with 80 ms exposure time, 2×2 binning, 16 phase steps, 670 V for MCP voltage, and an average laser power of 10% at 100 MHz. From the images calculated for A, I, and Φ, a line scan over the edge is extracted as if a point detector had been scanned over the phantom with the source coaxially. This is done in this way that, for every source position in the images, the signal of a virtual point detector can be calculated, i.e., the signal in a certain ROI of $5\times5=25$ pixels is averaged, corresponding to the position of the source [Fig. 12(a)].

The totally absorbing layer shows a typical signal course in amplitude and phase as it can be observed in measurements with a point detector.[50] The normalized $A_{\mathrm{norm}}=A/\max\{A\}$ starts getting smaller approximately 10 mm before the edge [Fig. 12(d)]. At approximately 10 mm behind the edge, the signal falls onto the noise level. No distinct difference can be seen in the signal course with increasing frequency. The intensity part shows the same behavior.

The phase gets smaller closer to the edge and quickly rises behind it [Fig. 12(e)]. With the frequency increasing, in the normalized phase $\Phi_{\mathrm{norm}}=\Phi-\Phi_{x=-18\ \mathrm{mm}}$, a more distinct minimum can be seen in addition to a steeper increase behind the edge. At a point 10 mm behind the edge, the signal is too weak to determine the phase correctly.

The layer phantoms which had doubled absorption or

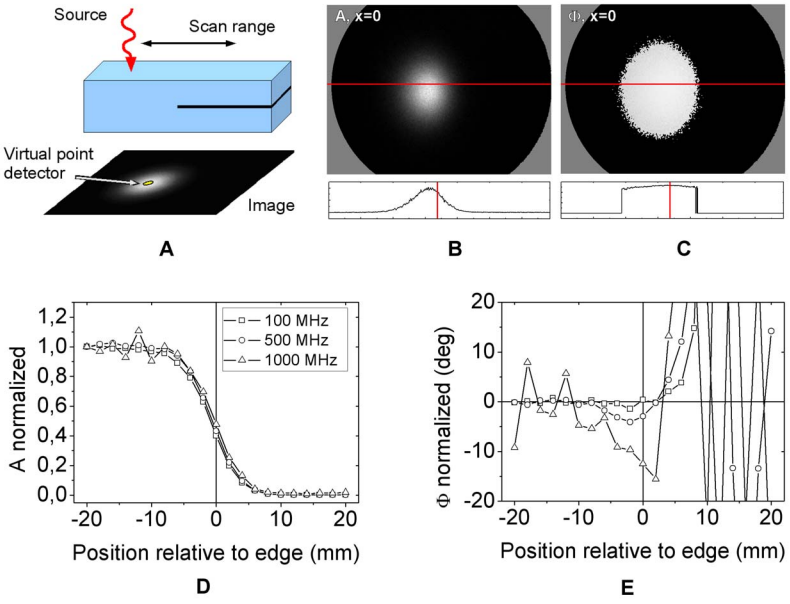

FIG. 12. (Color online) Laser scanned over the edge of totally absorbing layer inserted in a slab phantom, a coaxial line scan for twenty laser positions was extracted by calculating the mean in an ROI of 11×11 pixels at the laser position for each image as the reading of a virtual detector (A), amplitude (B), and phase (C) image with laser at the edge position ($x=0$), profiles extracted at marked horizontal line, edge/laser position marked with vertical line, line scan normalized at 100, 500, and 1000 MHz for amplitude (D) and phase (E).

scattering, with regard to the background optical properties, show only small changes in the signal in front of the edge and behind the edge.

To illustrate these changes, measurements were made at two source positions each 20 mm before and behind the edge in order to determine the contrast C. Contrast is simply defined by the difference between the signal at the position before (homogeneous part) and behind the edge (layer part). The definition example for amplitude is as follows:

$$C_A = \langle A_H \rangle - \langle A_L \rangle, \tag{5}$$

where index H denotes the "homogeneous" part and index L the "layer" part.

Signals were generated by averaging over an ROI of $11\times11=121$ pixels at these positions in the images. In addition, a contrast-to-noise ratio (CNR) was calculated. The definition example for amplitude is as follows:

$$\mathrm{CNR}_A = \frac{C_A}{\sigma_{\Delta A}} = \frac{\langle A_H \rangle - \langle A_L \rangle}{\sqrt{\sigma_H^2 + \sigma_L^2}}. \tag{6}$$

The noise σ is calculated from the standard deviation of signal fluctuation in the ROI. In the amplitude signal, contrast decreases slightly with frequency for both layers [Fig. 13(a)]. The contrast due to the scattering layer is a bit stronger. When the phase is considered [Fig. 13(b)], the value of contrast increases with frequency for both layers: for the absorbing layer with a positive sign and for the scattering layer with a negative sign. The CNR_A declines at higher frequencies [Fig. 13(c)] for both layers, whereas CNR_Φ shows a distinct maximum around 600 MHz [Fig. 13(d)]. In general, the CNR caused by the scattering layer is slightly higher than the one caused by the absorbing layer. In amplitude, it is in excess of 1 for almost the whole frequency range; in phase, a value of 1 or above is reached around the maximum only.

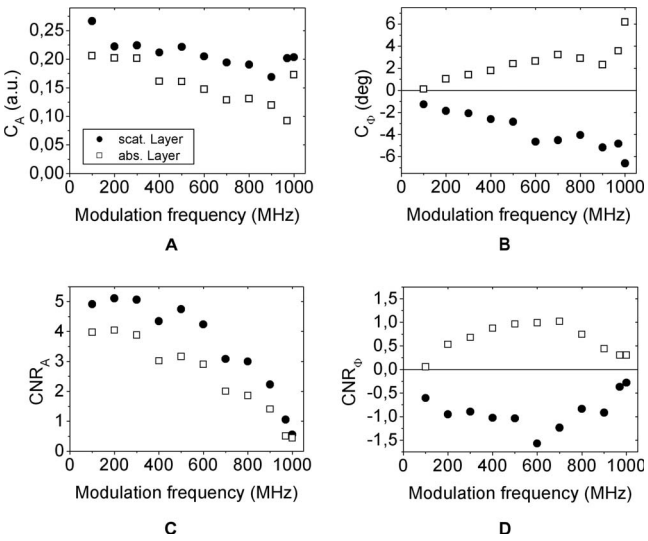

FIG. 13. Contrast of amplitude (A) and phase (B) on slab phantoms with layer with enhanced scattering and absorption, contrast-to-noise ratio of amplitude (C) and phase signal (D).

2. Finger joint phantom

Phantom design. A detailed finger phantom was developed to simulate different tissue components inside the phantom and to vary optical parameters of some components for simulation of rheumatoid arthritis (RA). In the early stages of RA, changes occur in the optical properties of the capsule, in the fluid in the joint gap, and inside the capsule volume.[51]

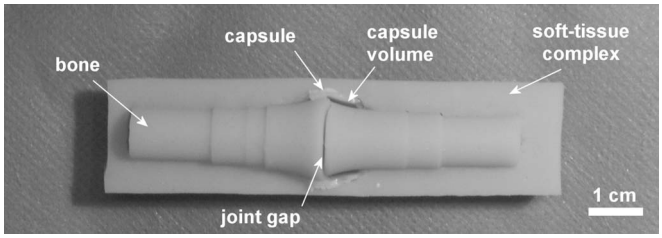

FIG. 14. Cylindrical finger joint phantom composed of solid components made of silicone and fluid filling the gaps (upper half of soft-tissue complex removed), simulation of healthy and diseased stage by changing the capsule and fluid having different optical properties, distal end (finger tip) left.

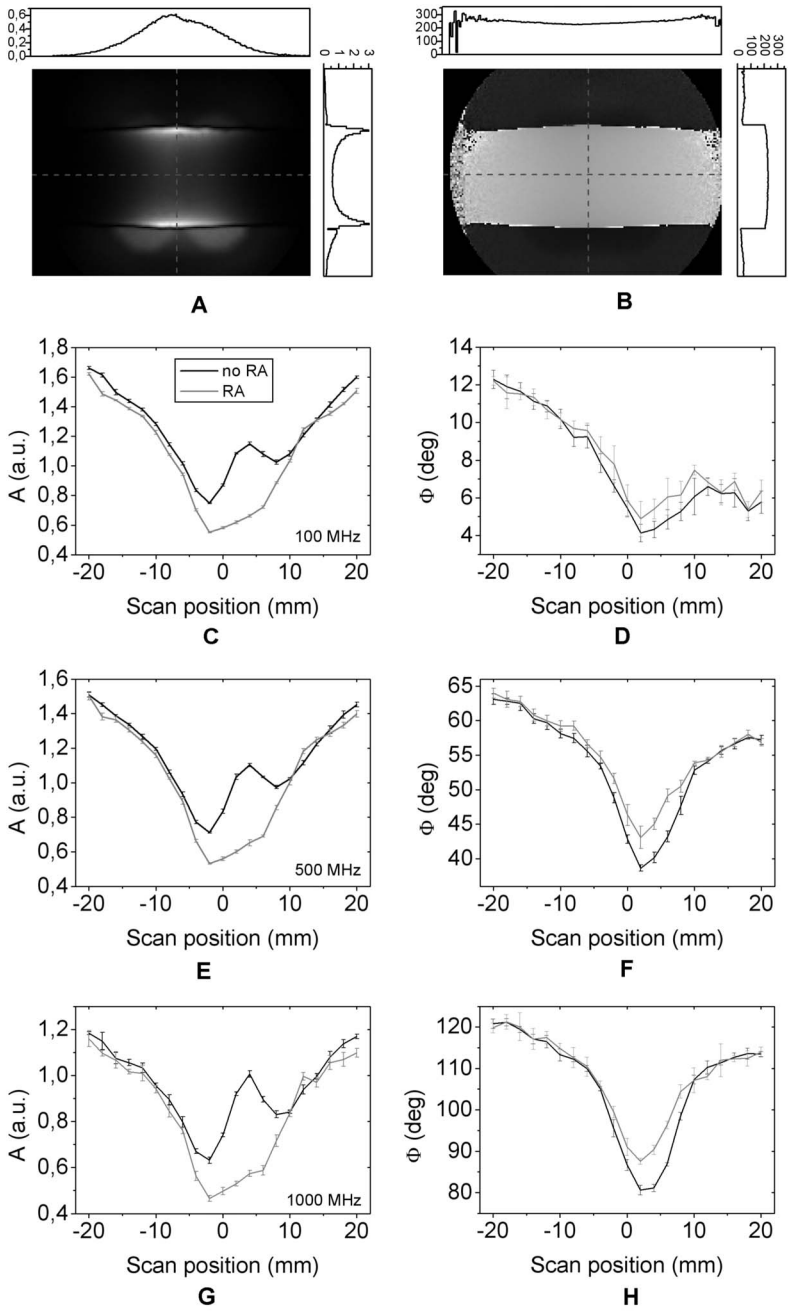

FIG. 15. Scan over the finger phantom, amplitude (A) and phase (B) image at 500 MHz with source at position $x=0$ mm with profiles extracted at marked lines. For two different stages simulating non-RA and RA coaxial scans were extracted from amplitude and phase images for 20 laser positions, for 100 MHz [(C) and (D)], 500 MHz [(E) and (F)], and 1000 MHz [(G) and (H)], error bars calculated by standard deviation from averaging over five measurements.

Therefore, our concept for the phantom was to combine bones, a capsule, a surrounding complex which represents the skin and other soft tissue, a joint gap, and a capsule volume (Fig. 14). The finger phantom was cylinder shaped with a diameter of 20 mm; a size which is typical for a proximal interphalangeal (PIP) joints of a human middle finger. Furthermore, the asymmetric shape of the bone ends and the capsule was implemented in the phantom design. The material for all solid phantom components was the same as for the slab phantom, however, with differing optical properties (Table II). The joint gap and the volume between capsule and bone were filled with a fluid composed of clear 60% glycerol in aqueous solution ($n=1.41$). A combination of ink (Pelikan 4001, brilliant black) and full milk was added to adjust absorbance and scattering. After assembling the phantom, it was wrapped in a transparent, self-sealing film.

Different joint properties. Two different stages of the finger joint phantom were evaluated, (1) the normal stage and (2) the inflamed RA stage. To test the sensitivity of the system to the different optical properties a scan with the laser was performed from the distal end (finger tip) to the proximal end (hand) over a line covering a range of 40 mm with step width of 2 mm. The finger phantom was placed in such a way so that the joint gap was located at the center of the source scan range. Measurements were taken with a 50 mm Nikon lens with $f/2$ at 100, 200, 400, 500, 600, 800, and 1000 MHz with 80 ms exposure time, 8×8 binning, 64 phase steps, and average laser power set to 30% at 100 MHz.

The phantom was scanned in the two different states each five times. A line scan was extracted from the images acquired as if the phantom was coaxially scanned by the

source and a single pixel detector in the same way as for the slab phantom. Mean and standard deviation were calculated from averaging over extracted line scans.

In Fig. 15 the results are shown for 100, 500, and 1000 MHz. The A and Φ scans show a distinct course over the phantom that demonstrates the influence of the different phantom parts and stages. In both A and Φ, there is a drop toward the middle of the joint. Because damping of modulation depends more on absorption than on scattering, the drop in A in the middle is caused by the higher absorption of the bone compared to the surrounding material and its increasing volume. The phase Φ indicates the time delay or path length of the detected light and should mainly depend on changes in scattering. As the bone and skin complex have the same scattering coefficient, the drop in Φ occurs because of the low scattering fluid in the capsule volume and the joint gap. In the normal situation, i.e., non-RA stage, the low absorption in the joint fluid and in the capsule volume causes a rise in amplitude in the capsule region. Therefore, A shows a local maximum in the region of the capsule. The phase is higher in the joint region for the RA stage when compared to the healthy joint. Noise from repeated measurements is very low.

Considering the differences of the line scans in the joint region, the determined p value for the amplitude satisfies a significance level below $\alpha=0.001$ for all frequencies. In phase, the significance level depends on the modulation frequency. It is below $\alpha=0.2$ for 100 MHz, where phase shift is very low, and $\alpha=0.002$ for frequencies beyond 100 MHz. Thus, amplitude and phase signal clearly enable to distinguish between the two stages.

IV. DISCUSSION AND CONCLUSION

We have reported on a new frequency-domain system for optical imaging that provides the capability for two-dimensional imaging of amplitude and phase up to 1 GHz. It was designed and tested for fast imaging of small geometries such as, for example, finger joints. The system tests show that precision is in the range of a few percent in amplitude but almost independent on frequency. Tests on frequency response of signal and noise show that the signal characteristics are in good agreement with measurements and theoretical predictions from other groups.[45,46,48] In general, amplitude decreases with increasing frequency whereas phase increases. The concrete frequency response of signal and noise always depends on the optical properties of the medium. The system enables measurements to be taken with sufficient SNR, in both amplitude and phase over a wide frequency range. The amplitude SNR decreases with increasing frequency but the phase SNR shows a maximum around 500–600 MHz as reported by Boas *et al.*[45] and Toronov *et al.*[46]

The minimum time required for a complete data acquisition is about 1.5 s. This means that for tomographic imaging the time for scanning over a certain number of source positions including data acquisition can be kept below 1 min. This is particularly important for clinical applications, because long measurement times are burdensome for patients and often reduces data quality because of motion artifacts.

A slab phantom with jointlike absorption and scattering showed that detection of a thin layer with enhanced absorption and scattering is possible. The signal change in amplitude is nearly the same whether if absorption or scattering is enhanced because in any case increase of one of these parameters causes damping of the amplitude. However, in phase, the signal changes with different signs for absorption and scattering. According to the results reported by Krämmer *et al.*,[48] the amplitude contrast slightly decreases with increasing frequency but increases in phase.

A finger joint phantom was built to simulate changes in optical properties occurring in rheumatoid arthritis (RA). It was tested by simulating two different stages, healthy and inflamed as in early RA. Simple line scans over the joint regions showed that the small changes between these two stages are distinguishable with $p<0.001$ in amplitude over the whole frequency range and $p<0.002$ in phase beyond 100 MHz.

The results verify that, for evaluation of pathological changes in tissue, frequency-domain optical imaging can be more valuable compared to continuous wave imaging because amplitude and phase are sensitive to changes of the optical properties and, particularly, phase carries additional information about the type of change. For small geometries and jointlike properties, the optimal frequency range is around 500–600 MHz. The best SNR in phase lies in this range and the SNR in amplitude is still sufficiently large.

ACKNOWLEDGMENTS

This work was supported by Grant No. 2R01 AR46255 from the National Institute of Arthritis and Musculoskeletal and Skin Diseases, USA, which is part of the National Institutes of Health.

[1] *Optical Tomography and Spectroscopy of Tissue IV*, Proc. SPIE 4250, edited by B. Chance, R. R. Alfano, B. J. Tromberg, M. Tamura, and E. M. Sevick-Muraca (2001).
[2] *Optical Tomography and Spectroscopy of Tissue III*, Proc. SPIE 3597, edited by B. Chance, R. R. Alfano, and B. J. Tromberg (1999).
[3] *Optical Tomography and Spectroscopy of Tissue: Theory, Instrumentation, Model, and Human Studies II*, Proc. SPIE 2979, edited by B. Chance and R. R. Alfano (1997).
[4] *Optical Tomography, Photon Migration, and Spectroscopy of Tissue and Model Media: Theory, Human Studies, and Instrumentation*, Proc. SPIE 2389, edited by B. Chance and R. R. Alfano (1995).
[5] *Medical Optical Tomography: Functional Imaging and Monitoring*, SPIE Institutes for Advanced Optical Technologies Series Vol. IS11, edited by G. Müller, B. Chance, R. R. Alfano, S. Arridge, J. Beuthan, E. Gratton, M. Kaschke, B. Masters, S. Svanberg, and P. van der Zee (SPIE, Bellingham, Washington, 1993).
[6] J. R. Mourant, M. Canpolat, C. Brocker, O. Esponda–Ramos, T. M. Johnson, A. Matanock, K. Stetter, and J. P. Freyer, J. Biomed. Opt. **5**, 131 (2000).
[7] J. R. Mourant, A. H. Hielscher, A. A. Eick, T. M. Johnson, and J. P. Freyer, Cancer Cytopathology **84**, 366 (1998).
[8] J. R. Mourant, J. P. Freyer, A. H. Hielscher, A. A. Eick, D. Shen, and T. M. Johnson, Appl. Opt. **37**, 3586 (1998).
[9] Y. Xu, H. L. Graber, and R. L. Barbour, Appl. Opt. **46**, 1693 (2007).
[10] J. C. Hebden and T. Austin, Eur. Radiol. **17**, 2926 (2007).
[11] D. K. Joseph, T. J. Huppert, M. A. Franceschini, and D. A. Boas, Appl. Opt. **45**, 8142 (2006).
[12] X. Zhang, V. Y. Toronov, and A. G. Webb, Rev. Sci. Instrum. **77**, 114301 (2006).
[13] D. R. Leff, O. Warren, L. C. Enfield, A. P. Gibson, T. Athanasiou, D. K. Pattern, J. C. Hebden, G. Z. Yang, and A. Darzi, "Diffuse optical imaging

of the healthy and diseased brease — A systematic review," Breast Cancer Res. Treat. (to be published).
[14] G. Boverman, Q. Fang, S. A. Carp, E. L. Miller, D. H. Brooks, J. Selb, R. H. Moore, D. B. Kopans, and D. A. Boas, Phys. Med. Biol. **52**, 3619 (2007).
[15] C. Li, H. Zhao, B. Anderson, and H. Jiang, Med. Phys. **33**, 627 (2006).
[16] B. W. Pogue, S. Jiang, H. Dehghani, C. Kogel, S. Soho, S. Srinivasan, X. Song, T. D. Tosteson, S. P. Poplack, and K. D. Paulsen, J. Biomed. Opt. **9**, 541 (2004).
[17] Q. Zhu, C. Xu, P. Guo, A. Aguirre, B. Yuan, F. Huang, D. Castilo, J. Gamelin, S. Tannenbaum, M. Kane, P. Hegde, and S. Kurtzman, Technol. Cancer Res. Treat. **5**, 365 (2006).
[18] Q. Zhang, T. J. Brukilacchio, A. Li, J. J. Stott, T. Chaves, E. Hillman, T. Wu, M.-A. Chorlton, E. Rafferty, R. H. Moore, D. B. Kopans, and D. A. Boas, J. Biomed. Opt. **10**, 024033 (2005).
[19] X. Intes, Acad. Radiol. **12**, 934 (2005).
[20] R. Choe, A. Corlu, K. Lee, T. Durduran, S. D. Konecky, M. Grosicka–Koptyra, S. R. Arridge, B. J. Czerniecki, D. L. Fraker, A. DeMichele, B. Chance, M. A. Rosen, and A. G. Yodh, Med. Phys. **32**, 1128 (2005).
[21] C. H. Schmitz, D. P. Klemer, R. Hardin, M. S. Katz, Y. Pei, H. L. Graber, M. B. Levin, R. D. Levina, N. A. Franco, W. B. Solomon, and R. L. Barbour, Appl. Opt. **44**, 2140 (2005).
[22] X. Gu, Q. Zhang, M. Bartlett, L. Schutz, L. L. Fajardo, and H. Jiang, Acad. Radiol. **11**, 53 (2004).
[23] Q. Zhang and H. Jiang, Opt. Lasers Eng. **43**, 1237 (2005).
[24] A. K. Scheel, M. Backhaus, A. D. Klose, B. Moa–Anderson, U. Netz, K. G. Hermann, J. Beuthan, G. A. Müller, G. R. Burmester, and A. H. Hielscher, Ann. Rheum. Dis. **64**, 239 (2005).
[25] A. H. Hielscher, A. D. Klose, A. K. Scheel, B. Moa–Anderson, M. Backhaus, U. Netz, and J. Beuthan, Phys. Med. Biol. **49**, 1147 (2004).
[26] Y. Xu, N. V. Iftimia, H. Jiang, L. L. Key, and M. B. Bolster, Opt. Express **8**, 447 (2001).
[27] X. Intes and B. Chance, Radiol. Clin. North Am. **43**, 221 (2005).
[28] H. Zhao, F. Gao, Y. Tanikawa, K. Homma, and Y. Yamada, Appl. Opt. **44**, 1905 (2005).
[29] A. Torricelli, V. Quaresima, A. Pifferi, G. Biscotti, L. Spinelli, P. Taroni, M. Ferrari, and R. Cubeddu, Phys. Med. Biol. **49**, 685 (2004).
[30] J. B. Fishkin, E. Gratton, M. J. vandeVen, and W. W. Mantulin, Proc. SPIE **1431**, 122 (1991).
[31] B. Chance, J. S. Leigh, H. Miyake, D. S. Smith, S. Nioka, R. Greenfeld, M. Finander, K. Kaufmann, W. Levy, M. Young, P. Cohen, H. Yoshioka, and R. Boretsky, Proc. Natl. Acad. Sci. U.S.A. **85**, 4971 (1988).
[32] F. E. W. Schmidt, M. E. Fry, E. M. C. Hillman, J. C. Hebden, and D. T. Delpy, Rev. Sci. Instrum. **71**, 256 (2000).
[33] A. P. Gibson, J. C. Hebden, and S. R. Arridge, Phys. Med. Biol. **50**, R01 (2005).
[34] J. C. Hebden, S. R. Arridge, and D. T. Deply, Phys. Med. Biol. **42**, 825 (1997).
[35] A. H. Hielscher, A. Y. Bluestone, G. S. Abdoulaev, A. D. Klose, J. Lasker, M. Stewart, U. Netz, and J. Beuthan, Dis. Markers **18**, 313 (2002).
[36] J. P. Culver, R. Choe, M. J. Holboke, L. Zubkov, T. Durduran, A. Slemp, V. Ntziachristos, B. Chance, and A. G. Yodh, Med. Phys. **30**, 235 (2003).
[37] B. Brooksby, S. Jiang, H. Dehghani, B. W. Pogue, K. D. Paulsen, C. Kogel, M. Doyley, J. B. Weaver, and S. P. Poplack, Rev. Sci. Instrum. **75**, 5262 (2004).
[38] T. O. McBride, B. W. Pogue, S. Jiang, U. L. Osterberg, and K. D. Paulsen, Rev. Sci. Instrum. **72**, 1817 (2001).
[39] I. Nissilä, T. Noponen, K. Kotilahti, T. Katila, L. Lipiainen, T. Tarvainen, M. Schweiger, and S. Arridge, Rev. Sci. Instrum. **76**, 044302 (2005).
[40] K. W. Berndt and J. R. Lakowicz, Proc. SPIE **1431**, 149 (1991).
[41] E. M. Sevick, J. R. Lakowicz, H. Szmacinski, K. Nowaczyk, and M. L. Johnson, J. Photochem. Photobiol., B **16**, 169 (1992).
[42] J. S. Reynolds, T. L. Troy, and E. M. Sevick–Muraca, Biotechnol. Prog. **13**, 669 (1997).
[43] T. French, J. Maier, and E. Gratton, Proc. SPIE **1640**, 254 (1992).
[44] X. Gu, K. Ren, and A. H. Hielscher, Appl. Opt. **46**, 1624 (2007).
[45] D. A. Boas, M. A. O'Leary, B. Chance, and A. G. Yodh, Appl. Opt. **36**, 75 (1997).
[46] V. Toronov, E. D'Amico, D. Hueber, E. Gratton, B. Barbieri, and A. Webb, Opt. Express **11**, 2717 (2003).
[47] M. S. Patterson, B. W. Pogue, and B. C. Wilson, in *Medical Optical Tomography: Functional Imaging and Monitoring*, SPIE Institutes for Advanced Optical Technologies Series Vol. IS11, edited by G. Müller, B. Chance, R. Alfano *et al.* (SPIE, Bellingham, WA, 1993), p. 513.
[48] P. Krämmer, H. Bartelt, H. Fischer, and B. Schmauß, Proc. SPIE **2326**, 65 (1995).
[49] L. Montandon, D. Salzmann, F. Bevilacqua, and C. Depeursinge, Proc. SPIE **3566**, 236 (1998).
[50] U. J. Netz, A. K. Scheel, A. H. Hielscher, and J. Beuthan, Laser Phys. **17**, 453 (2007).
[51] V. Prapavat, R. Schütz, W. Runge, J. Beuthan, and G. J. Müller, Proc. SPIE **2626**, 121 (1995).